

# We are IntechOpen, the world's leading publisher of Open Access books Built by scientists, for scientists

6,900

Open access books available

186,000

International authors and editors

200M

Downloads

Our authors are among the

154

Countries delivered to

TOP 1%

most cited scientists

12.2%

Contributors from top 500 universities



WEB OF SCIENCE™

Selection of our books indexed in the Book Citation Index  
in Web of Science™ Core Collection (BKCI)

Interested in publishing with us?  
Contact [book.department@intechopen.com](mailto:book.department@intechopen.com)

Numbers displayed above are based on latest data collected.  
For more information visit [www.intechopen.com](http://www.intechopen.com)



---

# BaTiO<sub>3</sub>:H Films as All-Solid-State Electrolytes for Integrated Electric Double-Layer Capacitors

---

Fadhel El Kamel

Additional information is available at the end of the chapter

<http://dx.doi.org/10.5772/65110>

---

## Abstract

In the electric double-layer capacitors (EDLCs), a large amount of electrical energy can be stored in the double layer by reversible accumulation of ions onto the active electrode material. In these devices, mobile charge carriers can accumulate (or deplete) near the electrode/electrolyte interface resulting in a space charge layer. So, the appropriate combination of space charge layer and large effective surface of the electrodes constitutes a significant factor to get high specific capacitance. Here, we incorporated protons in BaTiO<sub>3</sub> films during a low-temperature deposition process. Drastic changes occurred on both chemical and electrical properties of the films when H<sub>2</sub> was added to the sputtering gas. It is well known that protons are very mobile species even at low temperature. Therefore, upon the application of a sufficiently high electric field, positively charged protons move toward the cathode with an activation energy around 0.6 eV and pileup to form a capacitive double layer of several  $\mu\text{F}/\text{cm}^2$  which enhances the dielectric permittivity of the film.

**Keywords:** hydrogenated BaTiO<sub>3</sub> films, double layer, all-solid-state supercapacitors

---

## 1. Introduction

Owing to the progress in thin-film technology and materials engineering, electronic chips now integrate several functions on the same area, especially in wireless sensor networks, portable equipments, and other microsystems. As a result, microenergy sources need to be developed in order to drive such integrated electronic devices or to provide power during the temporary failure of the primary power sources. Two major performance criteria for any electrical energy storage device are required, energy and power densities. The first is defined as the amount of

energy stored per unit mass ( $\text{Wh/kg}$ ) or per unit volume ( $\text{Wh/m}^3$ ) in the device. The latter is a measurement of how fast energy is extracted from, or transferred into, the device per unit mass ( $\text{W/kg}$ ) or per unit volume ( $\text{W/m}^3$ ). The two criteria are particularly important where there is an excessive requirement for portability. Therefore, supercapacitors and Li-ion batteries should not necessarily be seen as competitors, because their charge storage mechanisms and thus their characteristics are different. Batteries convert chemical energy directly to electrical energy, in which charge is generated by redox reaction at electrodes and voltage is established between cell terminals depending on the chemical species and their concentrations. In previous batteries, this energy transformation is irreversible, but in novel ones, the chemical reaction is reversible, and thus the battery can be charged by supplying electrical energy to the cell.

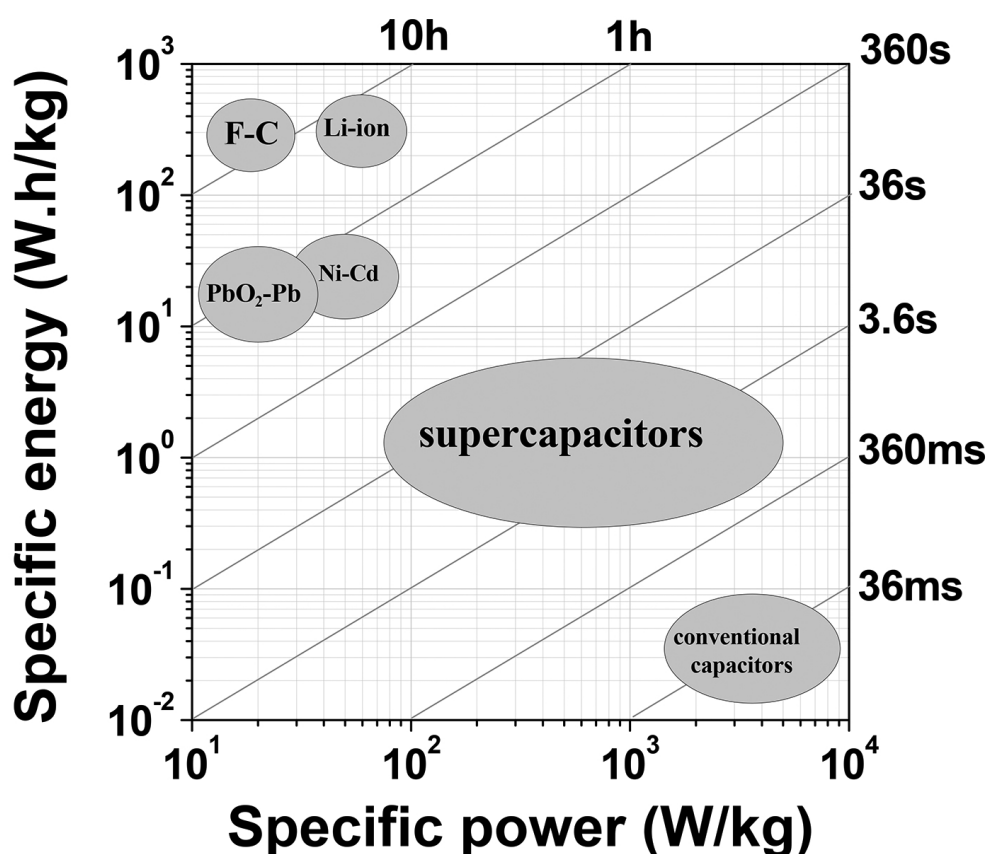


**Figure 1.** Specific power vs. specific energy (*Ragone plot*) for various electrical energy storage devices. Time constant values of each device are obtained by dividing the energy density by the power density.

Generally, the capacitance obtained with conventional capacitors finds its origin in the electronic, ionic, and dipolar polarization occurring in the bulk, whereas the essential reasons for electrical energy storage in supercapacitors are achieved by both the heavy load of electrode material per unit area and the relatively large specific capacitance of the electrolyte material. Supercapacitors can principally be classified as either electric double-layer capaci-

tors (EDLCs) or pseudocapacitors. The energy storage mechanism in the former devices relies on the separation of charges at the electrode/electrolyte interface, whereas in the latter, a faradic process occurs in addition to a simple charge separation. This feature explains why the charge storage capacity of pseudocapacitors is typically larger than that of EDLCs.

The availability of the stored charge will always be faster for supercapacitor (*surface storage*) than for a Li-ion battery (*bulk storage*), with a larger stored energy for the latter [1]. Both devices must be used in their respective time-constant domains (**Figure 1**).

Using a Li-ion battery for repeated high-power delivery/uptake applications for a short duration (less than 10 s) will quickly degrade the cycle life of the system. The only way to avoid this is to oversize the battery, increasing the cost and volume. In the same way, using supercapacitors for power delivery longer than 10 s requires oversizing.

Supercapacitors [2, 3], until now consisting of liquid-state electrolytes, have been widely regarded as energy storage devices for several electronic systems. Hence, they can ensure this power request since they have high-power density, which can be supplied in a very short time. Pseudocapacitive metal oxides (RuO<sub>2</sub>) [4, 5], conducting polymers [6], and carbon-based materials such as carbon nanotubes [7], graphite oxides [8], onion-like carbon [9], and activated carbon [10] have been widely reported in literature as electrode materials especially for liquid-state supercapacitors with interdigital fingers [4, 9, 11] and roll-like [12] and sandwich [8] shapes. To date, these supercapacitors are principally based on liquid-state electrolytes, such as aqueous or organic solutions, and display high capacitance values (from 1 to 100 mF/cm<sup>2</sup>), according to the electrode nature and its geometry, the number of interdigitated microelectrodes in the device, the electrolyte, and so on. However, these devices cannot be used at high temperatures, because the aqueous or organic electrolytes undergo decomposition. In addition, they exhibit leakage current and ionic conductivity which vary significantly with temperature and frequency.

Although solid electrolytes are characterized by lower ionic conductivity compared to their liquid counterparts, we can overcome this drawback by decreasing the thickness of solid electrolytes [13] in order to reduce the diffusion path of charged ionic species or by increasing the effective electrode surface by using porous materials [14]. On the other hand, with solid-state electrolyte, supercapacitors have wide operational temperature range and negligible leakage current. Hydrogel-polymer electrolyte has been reported by Kaempgen et al. [15] for the all-solid-state supercapacitors. The estimated cell capacitance was around 1 mF/cm<sup>2</sup>, but the operating voltage range is limited to 1 V, making them nonfunctional for most applications. Yoon et al. [5] have investigated the use of a pseudocapacitive amorphous RuO<sub>2</sub> electrode with a Li<sub>x</sub>PO<sub>y</sub>N<sub>z</sub> (LiPON) solid electrolyte for the elaboration of a thin-film supercapacitor. They reported a specific capacitance of about 3.5 mF/cm<sup>2</sup>×μm and a high operating voltage range. However, the fast capacitance degradation observed after several charge/discharge cycles derives from the lower ion mobility of Li<sup>+</sup> ions in the LiPON electrolyte than that of H<sup>+</sup> and OH<sup>-</sup> ions in the liquid electrolyte. This suggests that solid electrolyte with high protonic conductivity holds promise for thin-film supercapacitor with high capacitance and high cycle life. Recently, solid-state electrolytes such as hydrated lithium fluoride [2], yttria-stabilized zirconia [3], and Ta<sub>2</sub>O<sub>5</sub>:H [16] are examples of ionic conductors investigated for such a purpose.

The deposition of solid-state supercapacitors reported up to now involves high-temperature processing [5, 17] or humidified environment [2]. This constitutes a serious limitation to integrate supercapacitors in electronic chips. As an alternative, here protons were incorporated in barium titanate ( $\text{BaTiO}_3$ ) films during a low-temperature deposition process. The main purpose of this study was focused on related electrical defects. We emphasize that drastic changes occur on both chemical and electrical properties of the films when  $\text{H}_2$  is added to the sputtering gas. The electric double-layer capacitance can reach values up to several  $\mu\text{F}/\text{cm}^2$ .

## 2. Experimental details

Barium titanate films were grown by rf magnetron sputtering process on gold, copper, and carbon nanowalls/Pt-coated silicon substrates (*previously coated with a chromium adhesion layer*). Film thickness is around  $1\ \mu\text{m}$  as measured by a Veeco Dektak 6 M surface profiler and confirmed by a scanning electron microscopy. During deposition the substrates were water cooled (*room temperature deposition*). Standard sputtering was performed with pure argon. Here, hydrogen was incorporated in the  $\text{BaTiO}_3$  layers during their growth by introducing  $\text{H}_2$  in the sputtering gas [ $\text{H}_2/(\text{H}_2 + \text{Ar})$  varies from 0 to 30 %]. The stoichiometry of the sputtering gas ( $\text{H}_2 + \text{Ar}$ ) was controlled using respective mass flows for each gas (*Ar and H<sub>2</sub>*). Since the films are grown at low temperature, they are found to be amorphous, as detected by X-ray diffraction.

Electrical and dielectric measurements were performed, in a dark-shielded cell filled with dry nitrogen, on M/a- $\text{BaTiO}_3$ :H/M (M = Au, Cu) planar capacitors, where gold and copper electrodes ( $1.77\ \text{mm}^2$  area) were evaporated through a shadow mask on the front side of the deposited films. Dielectric properties of these devices were studied as a function of temperature and frequency using a Novocontrol impedance analyzer (*with an ac test voltage of 100 mV*).

The capacitance (C), conductance (G), and dissipation factor ( $\tan\delta = G/C\omega$ ) were measured from  $10^{-1}$  to  $10^6$  Hz. Known the geometrical factor (*top electrode diameter and film thickness*), the dielectric constant  $\epsilon'$  and conductivity  $\sigma$  can be determined, and results will be presented as  $\epsilon'(f)$ ,  $\tan\delta(f)$ , and  $\sigma(f)$  plots. Current-voltage measurements were performed using a Keithley 6517A electrometer. Temperature variation was controlled by a Linkam hot stage.

## 3. Results and discussion

Films grown under pure argon are transparent [18]. This transparency diminishes widely with the addition of hydrogen in the sputtering gas. The color of hydrogenated films tends gradually to yellow and then to brown, and finally they darken for hydrogen mixing ratio (HMR) around 25 %. This dark color indicated a high oxygen deficiency [19, 20]. In order to better understand this color change, optical absorbance spectrum was recorded on the hydrogenated barium titanate films at room temperature using a Shimadzu (UV-3101 PC) UV-Vis-NIR scanning spectrophotometer in diffuse reflection mode. Amorphous barium

titanate is reported as a direct band gap material. So, it is evident that in the shorter wavelength region, the absorption coefficient  $\alpha$  follows a power law:

$$\alpha hv = B\sqrt{hv - E_0} \quad (1)$$

where  $hv$  is the energy of the incident photon,  $B$  is the absorption edge width parameter, and  $E_0$  is the optical band gap. Tauc plots [ $(\alpha hv)^2$  vs.  $hv$ ] for BaTiO<sub>3</sub>:H films are shown in Figure 2.

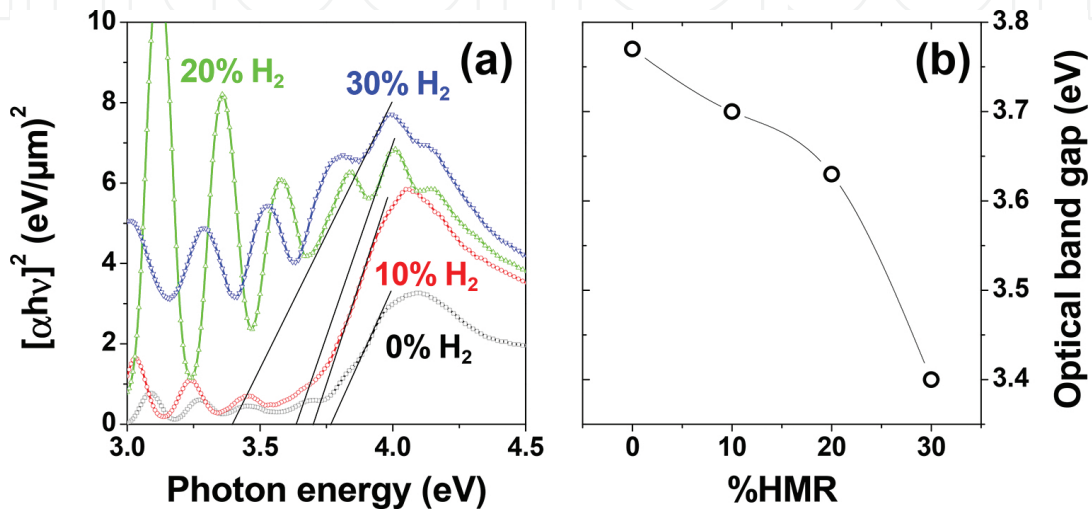


**Figure 2.** (a) UV-Vis absorbance spectra of hydrogenated barium titanate films deposited under different HMRs. Optical band gap energy was extracted by linear fit calculation. (b) Optical band gap energy as a function of HMR in the sputtering gas.

The linear fit of the straight-line portion of the data indicates a direct band gap with an energy value varying from 3.76 to 3.40 eV when HMR varies from 0 to 30 %. The optical absorption in the UV region is mainly attributed to the electron transition from the valence band maximum to the conduction band minimum. So, a plausible explanation for the band gap narrowing can be the existence of several defect levels, oxygen vacancies, or other kinds of punctual defects, within the band gap.

Evidences for hydrogen incorporation were previously given by the Fourier transform infrared spectroscopy and X-ray photoelectron spectroscopy [21]. It is worth noting that the hydrogenated films display a large density of hydroxide compared to the standard films (*grown under pure argon*), while the density of oxide remains constant in both films. The incorporation of hydrogen in the films during the deposition process can explain this feature. As it is already established [22–24], the hydrogen ionizes to give an electron (*donor defect*) and a proton ( $H^+$ ) which combines with oxygen of the perovskite lattice to form hydroxide groups.

**Figure 3** shows an overview on the frequency spectra associated to the capacitance density  $C(f)$  (**Figure 3(a)**) and the conductivity  $\sigma(f)$  (**Figure 3(b)**) performed at room temperature on *a*-BaTiO<sub>3</sub>:H films grown under different hydrogen mixing ratios (HMRs) in the sputtering gas.

We note that as hydrogen was introduced with a content exceeding 10 %, films display (**Figure 3(a)**) hundred times higher permittivity ( $\sim 2500$ ) than that measured on films grown under pure argon ( $\sim 20$ ). The double layer is clearly evidenced, especially at low temperatures by a dispersive behavior of the capacitance accompanied by a relaxation peak (LT Relax) in the loss measurements (**Figure 4(a)**).

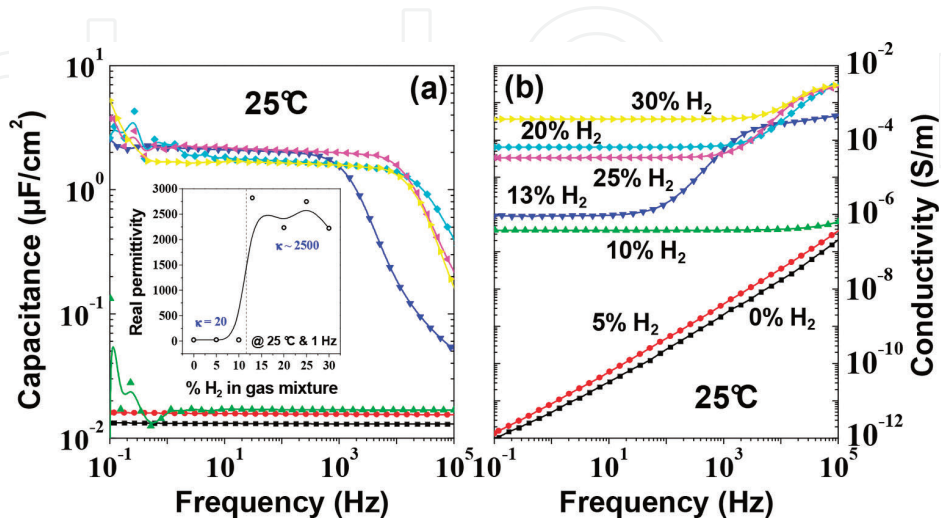


**Figure 3.** Frequency dependence of the capacitance density (a) and the conductivity (b) measured at room temperature on barium titanate layers sputtered under different hydrogen mixing ratios ranging from 0 to 30 %. The inset shows the variation of real permittivity vs. the hydrogen mixing ratios.

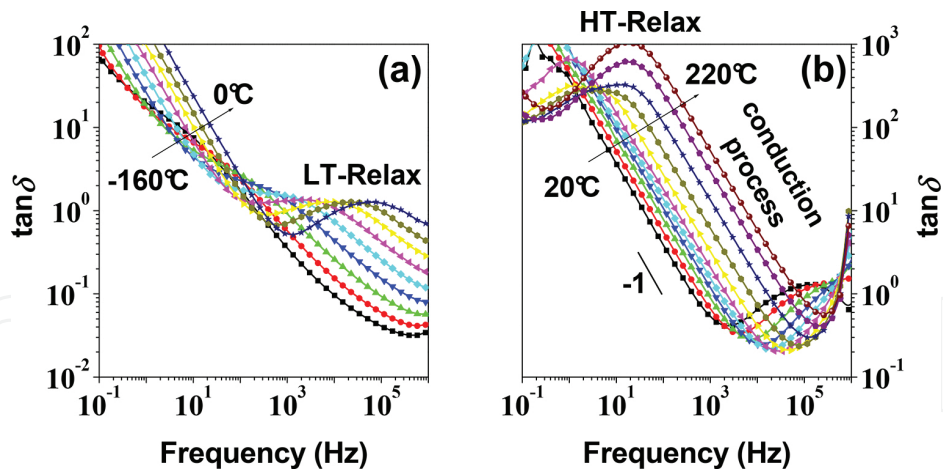


**Figure 4.** Temperature dependence of the loss factor  $\tan\delta(f)$ , measured on films grown under 25 % HMR. Data curve shows two relaxation peaks, which appear at low (LT Relax). (a) and high (HT Relax). (b) temperatures.

We believe that the dielectric losses are mainly the result of the ion migration and/or trap release. At high frequencies ( $f > 10$  kHz),  $C$  relaxes toward the bulk contribution, where mobile species cannot reach the electrodes under the ac test voltage (electrode polarization is basically a slow relaxation mechanism). As we can see in **Figure 3(a)**, the bulk capacitance of the hydrogenated films tends to the value measured when films were grown under pure argon.

The cutoff frequency ( $f = 10$  kHz) represents the speed of the capacitor [2] which constitutes an important parameter for both fundamental studies and technological applications. Furthermore, conductivity is also affected by the addition of hydrogen in the sputtering gas. At low frequency, it increases by up to eight orders of magnitude. The  $\sigma(f)$  characteristic shifts toward higher frequencies with the appearance of two plateaus, corresponding to the bulk and interfacial conductivities, that appear at high and low frequencies, respectively. This feature was previously [25] explained through the electrode polarization mechanism [26] which arises from proton accumulation at the cathode over a Debye length and gives rise to a large capacitance [25]. In the low-frequency domain, measured capacitance was completely determined by the charge stored in the double layer. As a result, electric double-layer capacitors have been widely regarded as energy storage devices.

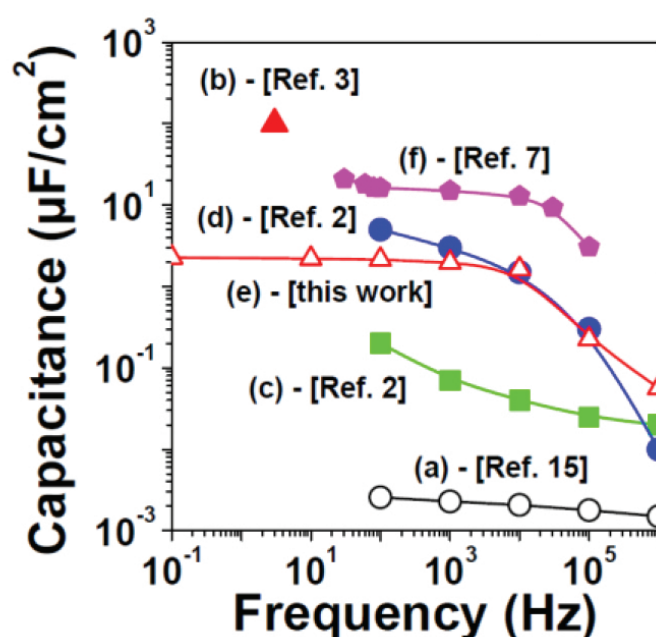


**Figure 5.** Selected literature data for the  $C(f)$  characteristics measured on different capacitors. (a) BaTiO<sub>3</sub> crystal (2 mm thick) sandwiched between two smooth metal electrodes. Protons are incorporated as mobile carriers by hydrogen charge for 8 days using electrolysis of water. (b) Ytria-stabilized zirconia (0.6 mm thick) sandwiched between two porous Pt/YSZ composite layers. Electric double layer is formed by the accumulation of oxygen ions. (c–d) Cu/LiF(0.32 μm thick)/Cu-based supercapacitor. Under the electric field, two charge carriers (Li<sup>+</sup> and F<sup>-</sup>) are accumulated at the interfaces. Measurements were carried out under two humid environments, 34 % RH (c) and 80 % RH (d). (e) *a*-BaTiO<sub>3</sub>:H (1 μm thick) sandwiched between two smooth Au electrodes (*the present work*). Electric double layer is formed by the accumulation of mobile proton carriers. (f) Solid-state supercapacitor from single-walled carbon nanotube arrays coated with Al<sub>2</sub>O<sub>3</sub>.

In general, electric double-layer capacitors (EDLCs) exhibit the property that a large electrical energy can be electrostatically stored in the double layer by reversible accumulation of ions (*from the electrolyte*) onto the active electrode material that is electrochemically stable. In these devices mobile charge carriers can accumulate or deplete near the electrode/electrolyte interface resulting in a space charge layer. So, the appropriate combination of space charge layer and large effective surface of the electrodes constitutes a significant factor to get high

specific capacitance. **Figure 5** shows selected literature data for the  $C(f)$  characteristics measured on different capacitors.

The most common devices at present use carbon-based active materials (*or other porous composite materials*) with high surface area as electrodes in EDLCs. In the present study, we used smooth metallic electrodes (*low surface area*) in order to study the effect of electrolyte without any contribution of the electrode nature in addition to carbon nanowall-coated platinum (CNW/Pt) as a high specific surface electrode. **Figure 6** displays the  $C(f)$ ,  $\varepsilon(f)$ , and  $\sigma(f)$  characteristics of Au/*a*-BaTiO<sub>3</sub>/Au (a), Au/*a*-BaTiO<sub>3</sub>:H/Au (c), and Au/*a*-BaTiO<sub>3</sub>:H/Cu (d) devices.

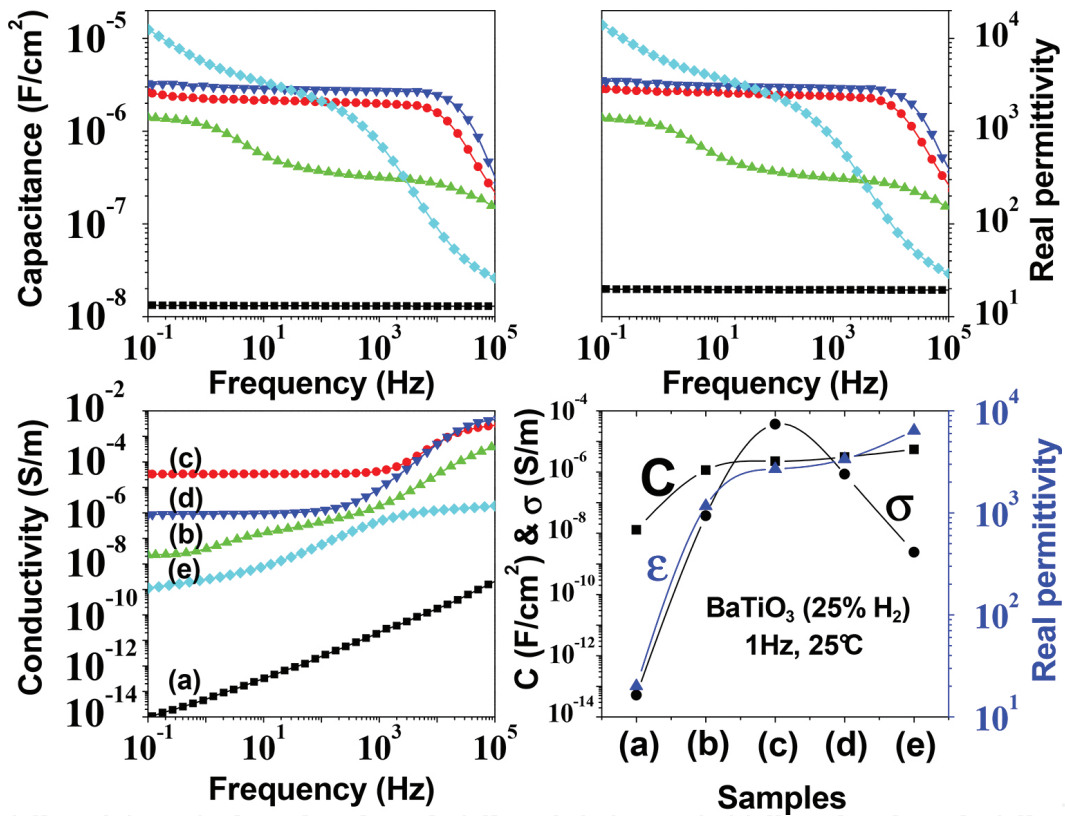


**Figure 6.**  $C(f)$ ,  $\varepsilon(f)$ , and  $\sigma(f)$  characteristics of (a) Au/*a*-BaTiO<sub>3</sub>/Au, (b) Au/*a*-BaTiO<sub>3</sub>/*a*-BaTiO<sub>3</sub>:H(20%H<sub>2</sub>)/*a*-BaTiO<sub>3</sub>/Au, (c) Au/*a*-BaTiO<sub>3</sub>:H(25%H<sub>2</sub>)/Au, (d) Au/*a*-BaTiO<sub>3</sub>:H(25%H<sub>2</sub>)/Cu, and (e) Au/*a*-BaTiO<sub>3</sub>:H(25%H<sub>2</sub>)/CNW/Pt devices. Even with low effective surface of electrodes, we can get acceptable values of capacitance that is higher than 2  $\mu\text{F}/\text{cm}^2$ , which leads to a real permittivity in the  $10^3$ – $10^4$  range.

We showed that even with low effective surface of electrodes, we can get acceptable values of capacitance that is higher than 2  $\mu\text{F}/\text{cm}^2$ , which leads to a real permittivity in the  $10^3$ – $10^4$  range. By increasing the surface area of the electrodes, we anticipate higher specific capacitance for our devices as observed with the Au/*a*-BaTiO<sub>3</sub>:H/CNW/Pt (e) device ( $C = 10 \mu\text{F}/\text{cm}^2$  and  $\varepsilon' = 10^4$  at low frequency).

To study the temperature dependence of the conduction mechanisms taking place in hydrogenated films, we plotted the relaxation frequencies  $f_0(T)$ , bulk  $\sigma_b(T)$ , and interfacial  $\sigma_i(T)$

conductivities, extracted from the relaxation peak position (Figure 4) and high- and low-frequency semicircles in the impedance diagram (Figure 7), respectively, as a function of  $1000/T$  (Arrhenius plot, Figure 8).

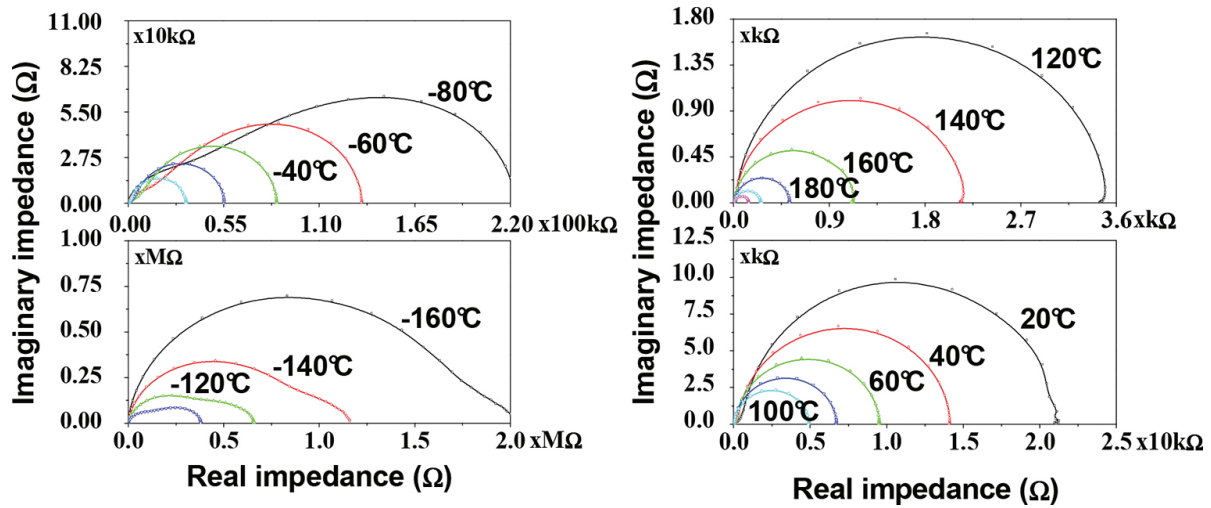


Figure 7. Complex impedance spectra ( $Z''-Z'$ ) carried out, at different temperatures, on hydrogenated barium titanate films. Samples were grown under 25 % HMR in the sputtering gas.

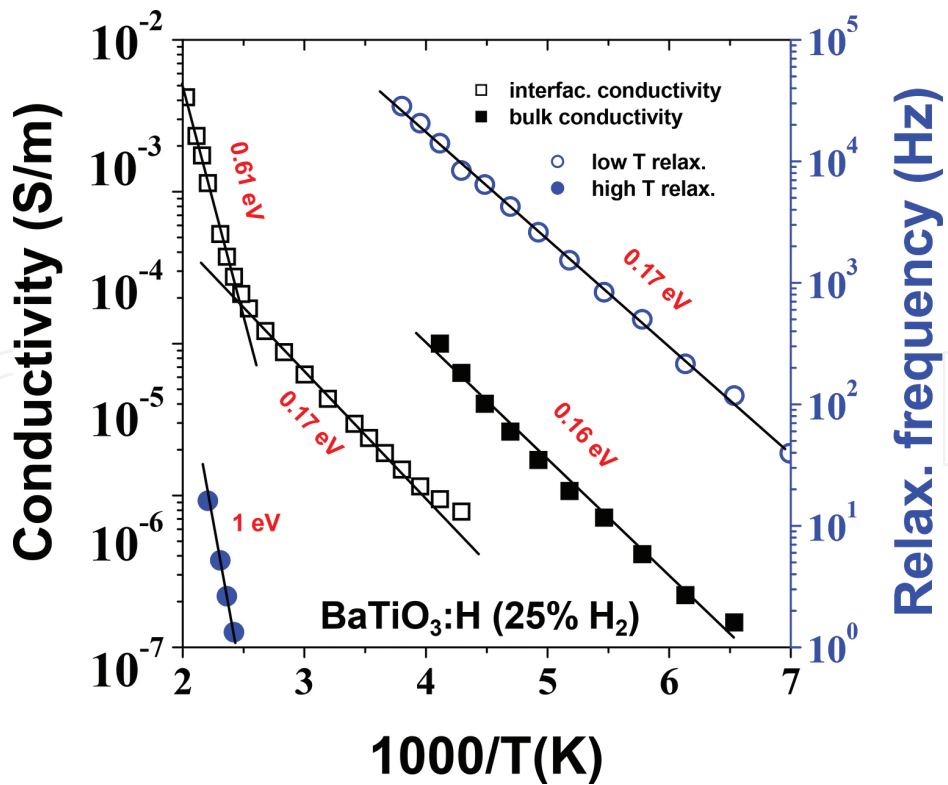
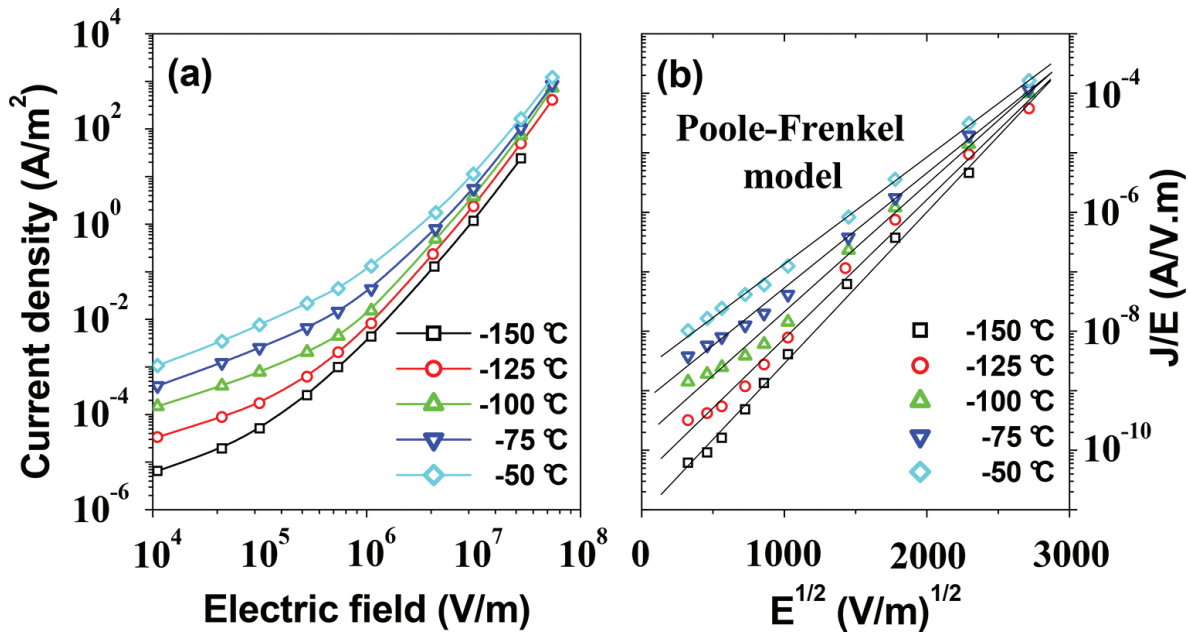


Figure 8. Relaxation frequency, bulk, and interfacial conductivities as a function of  $1000/T$  (Arrhenius diagram).

Measurements were carried out on samples grown under 25 % HMR in the sputtering gas. Both characteristics show the Arrhenius-type dependence over the whole temperature range, excluding the low-temperature ( $T < -100$  °C) interfacial conductivity. As shown in **Figure 8**, we can extract three activation energies which correspond to three different conduction processes.

I–V characteristics were recorded on hydrogenated films at different temperatures (from  $-150$  to  $-50$  °C) in order to explain the conduction mechanism in dc regime. DC bias was applied to the bottom electrode, and the current was measured after 60 s for stabilization concern. Experimental data measured on the Au/*a*-BaTiO<sub>3</sub>:H (17% HMR)/Au device are shown in **Figure 9(a)**.



**Figure 9.** (a) Temperature dependence of the leakage current (*J–E characteristics*). (b) *J–E characteristics* replotted according to the Poole-Frenkel model.

It is clearly seen that the leakage current density exhibits a Poole-Frenkel (PF)-type behavior, which implies that the conduction mechanism can be described by a thermally stimulated emission from a discrete set of traps. The PF model predicts that the current density can be expressed as:

$$J_{\text{PF}} = qN_c\mu E \exp\left(\frac{-q\left(\phi_t - \sqrt{qE / \pi\epsilon_{\text{opt}}}\right)}{k_B T}\right) \quad (2)$$

where  $E$  is the applied field,  $k_B$  is the Boltzmann constant,  $\mu$  is the electronic mobility,  $\epsilon_{\text{opt}}$  is the optical permittivity,  $q$  is the elementary charge,  $q\phi_t$  is the trap level, and  $N_c$  is the effective density of states in the conduction band assumed to be around  $10^{18}$  cm<sup>-3</sup> [27]. As stated above

(Poole-Frenkel *model*),  $\log(J/E)$  vs.  $E^{1/2}$  should be linear (**Figure 9(b)**). Then, we guess that the leakage current arises from the carriers release from shallow trap levels localized within the band gap. In order to determine this energy level, we plotted the current density vs.  $1/T$  at a fixed electric field.  $J$  vs.  $1/T$  curves (*not shown here*) display a linear behavior with a negative slope which suggests that the conduction process is thermally stimulated. Activation energy and carrier mobility vary, respectively, from 0.12 and  $4.30 \times 10^{-7}$  to 0.05 eV and  $2.00 \times 10^{-6}$  cm<sup>2</sup>/Vs when the electric field varies from 0.2 to 3.0 MV/m. Such energy values correspond to an electric-field-dependent effective trap depth  $[\phi_0 - \Delta\phi(E)]$ . Based on the slowness of the PF mechanism, these mobility values are in a good agreement with the electronic conduction. In the literature, electronic mobility shows a large discrepancy and is found to vary from  $10^{-3}$  [28–32] to  $10^{-10}$  cm<sup>2</sup>/Vs [27]. To determine the real trap's depth  $\phi_0$  (*at*  $E = 0$  V/m), we plotted the effective trap depths  $[\phi_0 - \Delta\phi(E)]$  as a function of  $E^{1/2}$  (**Figure 10**).

We found that the leakage current can be explained by the carrier release from shallow trap level  $\phi_0$  localized at around 0.15 eV below the conduction band. It is believed that positively charged protons can provide such energetic levels. It is interesting to note that the same amount of energy is required to activate the LT relaxation, bulk, and interfacial (*at*  $T < 120$  °C) conduction processes (**Figure 8**).

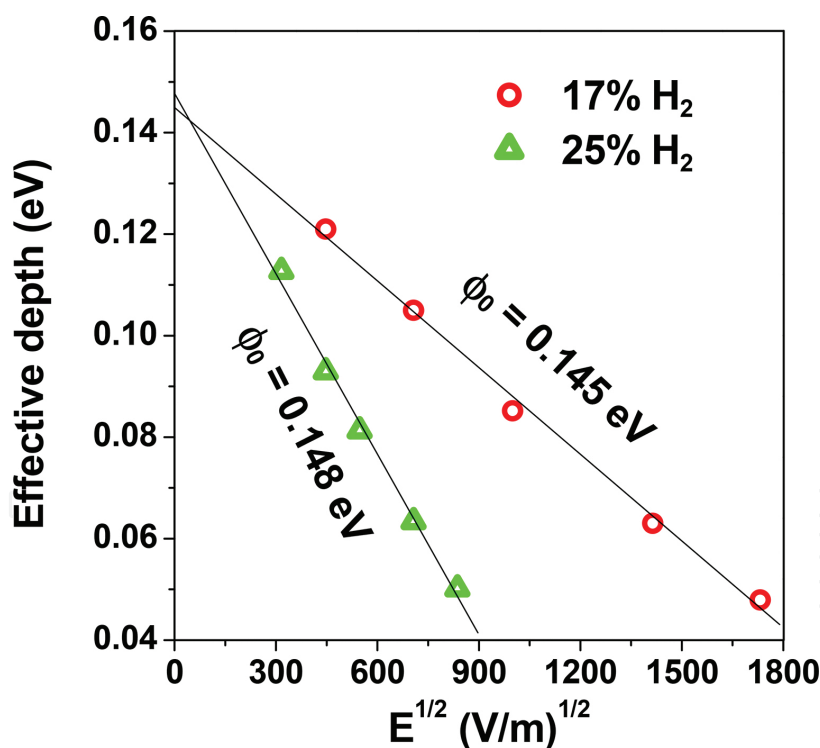


**Figure 10.** Effective trap depth as a function of  $E^{1/2}$ . Leakage currents can be explained by carrier detrapping from shallow trap level  $\phi_0$  localized at around 0.15 eV below the conduction band.

In amorphous materials, charged defects surrounding the proton tilt markedly the hydroxide group toward one of the neighboring oxygen ions. Oxygen vacancies constitute the main charged defects since the hydrogenated films were deposited under a reduced atmosphere.

They effectively act as positively charged defects that repel the proton. This feature allows the formation of a rather weak directional interaction (*hydrogen bond*) between the proton and one of the adjacent oxygen,  $O^{[1]}-H\sim O^{[2]}$  [33]. Such a site could be considered as a trap for protons. In this approach, electron issued from the ionization of hydrogen is weakly bonded, and it can be easily activated to the conduction band, from a shallow donor level estimated at around 0.15 eV, to increase the dielectric loss and the leakage current [34].

The hydrogen bond breakage can be responsible for a large proton conduction process in oxide materials. Several reports (*Ref. [35] and references therein*) adopted a model for O-H oscillators localized on regular oxygen sites and undergoing a stretching mode alongside the “O-O” direction. This situation allows small proton oscillations (*displacements to less than atomic spacing*). Due to their weakness, hydrogen bonds require an activation energy around 0.22 eV [36] to be dissociated even at low temperature. This value agrees well with the one (0.26 eV) determined previously [37] using dielectric measurements at temperature ranging from  $-25$  to  $-75$  °C (*not shown here*). Then, the dielectric response rising at that range can be ascribed to the dissociation of hydrogen bonds and consequently to a localized migration (*or oscillation*) of the protons alongside the hydroxide bond. Such process was previously emphasized and discussed by Weber et al. [35] in ionic conductor oxides.

Additionally, the interfacial conduction process considered at temperature higher than 120 °C for hydrogenated films was thermally activated with around 0.6 eV. It is whispered that the proton diffusion within oxide materials requires almost the same amount of energy. Actually, the reported activation energy should be strongly affected by the amorphous state of the material, but it agrees well with predicted experimental [38, 39] and theoretical [38–40] values (0.4–0.6 eV) for the best proton conductors such as Y-BaZrO<sub>3</sub> or BaCeO<sub>3</sub> [38, 39, 41]. Based on the experimental observation and on the light of literature mentioned above, the conduction mechanism is predominately of the Grotthuss type [42], that is, involving proton transfer (*hopping*) from the hydroxide defects to a nearest neighboring oxygen ion.

In order to better illustrate that the huge increase of the dielectric constant (**Figure 3**) arises from the accumulation of protons at the metal-BaTiO<sub>3</sub>:H interface (*double layer*), a tri-layer stack (BaTiO<sub>3</sub>/BaTiO<sub>3</sub>:H/BaTiO<sub>3</sub>) was grown by inserting the hydrogen-doped layer between two intrinsic thin layers. In that way, we can separate protons (*incorporated in hydrogenated layer*) from the metal electrode by an intrinsic (*proton free*) layer. The intrinsic layers (BaTiO<sub>3</sub>) were grown during 15 min under pure argon gas, whereas the hydrogenated layer (BaTiO<sub>3</sub>:H) was deposited during 90 min under Ar/H<sub>2</sub> gas mixture (80% Ar + 20 % H<sub>2</sub>) without breaking the deposition process. **Figure 11** reports the  $\epsilon'(f)$  and  $\sigma(f)$  characteristics measured at room temperature on barium titanate films deposited under different atmospheres (**Figure 11(a)**) and in different MIM structures (**Figure 11(b)**).

In **Figure 11(a)** gold was used as metal electrode, and curves labeled (A) were conducted on a sample grown under pure argon gas (*reference*), curves labeled (B) were carried out on a sample grown under 20 % HMR, and curves labeled (C) were done on a tri-layer stack (BaTiO<sub>3</sub>/BaTiO<sub>3</sub>:H/BaTiO<sub>3</sub>). Open symbols denote the dielectric constant  $\epsilon'$  and filled symbols represent the conductivity  $\sigma$ . In **Figure 11(b)** measurements were carried out on samples grown under 20 % HMR, where gold [*curves labeled (B)*] and copper [*curves labeled (D)*] were used as metal

electrodes. Further evidences that the observed frequency dispersion of the dielectric constant is related to the electrodes (*and not to the bulk*) are given. At low frequencies, we show that when an intrinsic layer between the hydrogenated bulk film and metallic electrodes was added, both the conductivity and the dielectric constant decrease while remaining higher compared to values measured on Ar-deposited films. This confirms that the low-frequency behavior is related to electrode effects. We previously [25] discussed the dispersive behavior of the  $\epsilon'(f)$  characteristic and attributed it to the proton migration. Protons are indeed very mobile species even at low temperature. Therefore, we can assume that upon the application of a sufficiently high electric field, the positively charged protons move toward the cathode and pile up to form a concentration gradient (*capacitive double layer*). The proton migration leads to an increase of the ionic conductivity and creates a capacitive double layer under the cathode which enhances the dielectric constant. In the case of tri-layer stack, the interfacial Ar-deposited layers react as *dead layers*, which reduce the capacitance of the MIM structure as observed at low frequencies.

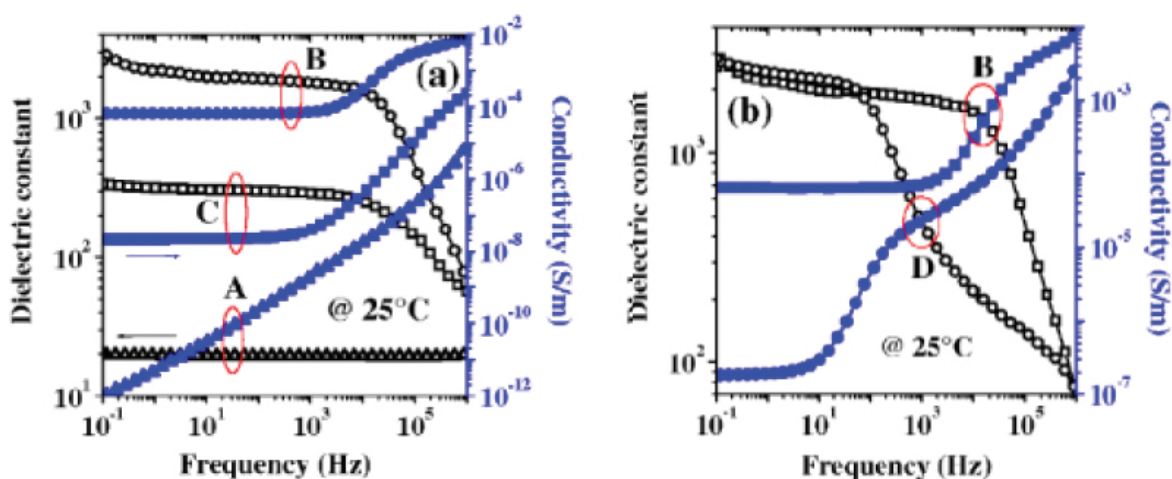


**Figure 11.** Frequency dependence of the dielectric constant and the conductivity. Measurements were carried out at room temperature on BaTiO<sub>3</sub>-based MIM capacitors grown under different (a) atmospheres and in different (b) MIM (M = Au, Cu) structures. Curves labeled (A) were conducted on a sample grown under pure argon gas (*reference*), curves labeled (B, D) were carried out on a sample grown under 20 % HMR, and curves labeled (C) were done on a tri-layer stack (BaTiO<sub>3</sub>/BaTiO<sub>3</sub>:H/BaTiO<sub>3</sub>). Open symbols denote the dielectric constant and filled symbols represent the conductivity.

To further check the influence of electrodes, the nature of the metal contact was varied (**Figure 11(b)**). Gold (Au/BaTiO<sub>3</sub>:H/Au) and copper (Cu/BaTiO<sub>3</sub>:H/Cu) were used as metal electrodes. It is seen that replacing the Au electrode by Cu is sufficient to modify the conductivity, especially in the low-frequency domain, where the conductivity measured on the Cu/BaTiO<sub>3</sub>:H/Cu decreases. This clearly shows that the dielectric response is strongly dependent on the electrode nature. Under an electric field, positively charged protons are drifted toward the cathode where, ideally (*if ohmic contact*), they are neutralized by electronic transfer through the electrode/electrolyte interface. In the case of bad charge transfer (*blocking contact*), mobile charges accumulate at the electrode/electrolyte interface, and a space charge region builds up at the electrode boundaries. This feature agrees with decreasing conductivity.

Finally, the last feature which can be observed in **Figure 8** is related to the HT relaxation process ( $T > 120\text{ }^{\circ}\text{C}$ ) which can be thermally activated by around 1 eV. This value is close to the usual activation energy reported for oxygen vacancy migration in titanates [43, 44]. These defects, resulting from the deposition under reduced atmosphere, are indeed very mobile species in titanates [43–45]. Therefore, we can assume that upon the application of a low-frequency electric field at sufficiently high temperature, the oxygen vacancies move toward the cathode and pile up at the interface to form a concentration gradient (*space charge*). This feature highly competes with the double layer previously formed by protons which leads to an increase of the electrical conduction with elapsed time.

## 4. Conclusion

Metal/*a*-BaTiO<sub>3</sub>:H(1 μm)/metal devices report a specific capacitance around 2 μF/cm<sup>2</sup>, steady in the frequency range from 0.1 to 10<sup>4</sup> Hz. This feature is suitable for ac circuits. On the other hand, these devices have low-temperature performance and are capable of delivering energy down to -100 °C with minimal effect on efficiency. Moreover, they can bear high voltages per cell. Compared to conventional capacitor technologies, the studied devices possess orders of magnitude higher energy density. This performance can be rather enhanced by using porous carbon electrodes to achieve a high surface area. In addition, these devices display a low internal resistance, hence providing acceptable power density capability compared to batteries. Finally, the deposition process seems to be compatible with easy incorporation of all-solid-state supercapacitors with other electronic devices. In addition, we can stack supercapacitors vertically to enhance the specific capacitance.

## Author details

Fadhel El Kamel

Address all correspondence to: elkf2000@yahoo.fr

LaPhyMNE, University of Gabès, Gabès, Tunisia

## References

- [1] B. E. Conway. *Electrochemical Supercapacitors: Scientific, Fundamentals and Technological Applications*. New York: Kluwer Academic/Plenum Publishers, 1999.
- [2] L. Ma et al. *Appl. Phys. Lett.* 2005;87:123503.
- [3] M. G. H. Hendriks et al. *J. Appl. Phys.* 2001;90:5303.

- [4] C. C. Liu et al. *Electrochim. Acta*. 2010;55:5768.
- [5] Y. S. Yoon et al. *J. Power Sources*. 2001;101:126.
- [6] J. H. Sung et al. *J. Power Sources*. 2003;124:343.
- [7] C. L. Pint et al. *Carbon*. 2011;49:4890.
- [8] W. Gao et al. *Nature Nanotech.*2011;6:496.
- [9] D. Pech et al. *Nature Nanotech.* 2010;5:651.
- [10] D. Pech et al. *J. Power Sources*. 2010;195:1266.
- [11] W. Sun et al. *J. Power Sources*. 2010;195:7120.
- [12] H. X. Ji et al. *Chem. Commun.* 2010;46:3881.
- [13] J. H. Lim et al. *J. Electrochem. Soc.* 2001;148:A275.
- [14] R. Kötz et al. *Electrochim. Acta*. 2000;45:2483.
- [15] M. Kaempgen et al. *Nano. Lett.* 2009;9:1872.
- [16] J. M. Lee et al. *J. Electroceram.* 2006;17:639.
- [17] J. M. Soon et al. *Electrochem. Solid-State Lett.* 2007;10:A250.
- [18] I. H. Pratt et al. *J. Vac. Sci. Technol.* 1970;8:256.
- [19] S. Furusawa et al. *Solid State Ionics*. 2005;176:553.
- [20] F. El Kamel et al. *J. European Ceram. Soc.* 2007;27:3807.
- [21] F. El Kamel et al. *Solid State Ionics*. 2009;180:853.
- [22] R. Waser. *J. Am. Ceram. Soc.* 1988;71:58.
- [23] J. Ahn et al. *Appl. Phys. Lett.* 2000;77:1378.
- [24] K. Xiong et al. *Appl. Phys. Lett.* 2004;85:2577.
- [25] P. Gonon et al. *Appl. Phys. Lett.* 2007;90:232902.
- [26] P. Gonon et al. *J. Appl. Phys.* 2007;101:073901.
- [27] Y. B. Lin et al. *J. Appl. Phys.* 2000;87:1841.
- [28] S. Zafar et al. *Appl. Phys. Lett.* 1998;73:175.
- [29] C. N. Berglund et al. *Phys. Rev.* 1967;157:358.
- [30] A. J. Moulson and J. M. Herbert. *Electroceramics: Materials, Properties and Applications*. London: Chapman and Hall; 1996.
- [31] D. Keroak et al. *J. Phys. C*. 1984;17:833.

- [32] J. P. Boyeaux et al. *J. Phys. C.* 1979;12:545.
- [33] L. Pejov. *Chem. Phys. Lett.* 2003;11:376.
- [34] L. Dobaczewski et al. *Phys. Rev. B.* 2004;69:245207.
- [35] G. Weber et al. *Phys. Rev. B.* 1986;34:8406.
- [36] J. O. M. Bockris and A. K. N. Reddy. *Modern Electrochemistry.* New York: Plenum; 1970.
- [37] F. El Kamel et al. *J. Vac. Sci. Technol. A.* 2012;30:04D110-1.
- [38] W. Münch et al. *Solid State Ionics.* 1999;125:39.
- [39] E. Matsushita et al. *Solid State Ionics.* 1997;97:45.
- [40] E. Matsushita et al. *Solid State Ionics.* 1999;125:31.
- [41] K. D. Kreuer. *Solid State Ionics.* 1999;125:285.
- [42] K. D. Kreuer. *Chem. Mater.* 1996;8:610.
- [43] F. El Kamel et al. *J. Appl. Phys.* 2006;99:094107.
- [44] R. Waser. *J. Am. Ceram. Soc.* 1989;72:2234.
- [45] R. Waser. *J. Am. Ceram. Soc.* 1991;74:1934.

IntechOpen